SWEDISH DEFENCE
RESEARCH AGENCY

FOI-R—0374--SE
March 2002
ISSN 1650-1942

Metodology report

Lars Olovsson

KRYP, a Finite Element Tool for Crystal Plasticity Analyses

Weapons and Protection
SE-147 25 Tumba

SWEDISH DEFENCE RESEARCH AGENCY
Weapons and Protection
SE-147 25 Tumba

FOI-R--0374--SE
March 2002
ISSN 1650-1942

Methodology report

Lars Olovsson

KRYP, a Finite Element Tool for Crystal Plasticity Analyses

Utgivare Totalförsvarets Forskningsinstitut - FOI Vapen och skydd 147 25 Tumba	**Rapportnummer, ISRN** FOI-R--07374--SE	**Klassificering** Metodrapport
	Forskningsområde 5. Bekämpning	
	Månad, år Januari 2002	**Projektnummer** I231
	Verksamhetsgren 5. Uppdragsfinansierad verksamhet	
	Delområde 51 VVS med styrda vapen	
Författare/redaktör Lars Olovsson	**Projektledare** Magnus Oskarsson	
	Godkänd av	
	Uppdragsgivare/kundbeteckning	
	Tekniskt och/eller vetenskapligt ansvarig	

Rapportens titel (i översättning)

KRYP, ett finita elementverktyg för kristallplasticitetsanalyser

Sammanfattning (högst 200 ord)

KRYP är ett finita elementverktyg för mesomekaniska kristallplasticitetssimularingar. Teorin är baserad på kontinuumsmekanik där dislokationer beskrivs med fältvariabler.

Syftet med projektet är att nå ett stadium där KRYP utvecklats till ett andvändbart verktyg för studier av korninteraktion och texturutveckling.

Utvecklingen av programvaran initierades i augusti 2001. Idag, ett halvt år senare, är KRYP ett funktionsdugligt finita elementprogram med en FCC kristallplasticitetsmodell som är färdig att utvärderas i detalj.

Nyckelord

kristallplasticitet, mesomekanik, kontinuumsmekanik

Övriga bibliografiska uppgifter	**Språk** Engelska
ISSN 1650-1942	**Antal sidor:** 30 s.
Distribution enligt missiv	**Pris: Enligt prislista**

Issuing organization
FOI – Swedish Defence Research Agency
Weapons and Protection
SE-147 25 Tumba

Report number, ISRN
FOI-R--0374--SE

Report type
Methodology report

Research area code
5. Combat

Month year
March 2002

Project no.
I231

Customers code
5. Commissioned Research

Sub area code
51 Weapons and Protection

Author/s (editor/s)
Lars Olovsson

Project manager
Magnus Oskarsson

Approved by

Sponsoring agency

Scientifically and technically responsible

Report title
KRYP, a Finite Element Tool for Crystal Plasticity Analyses

Abstract (not more than 200 words)

KRYP is a finite element program for meso-mechanical crystal plasticity simulations. The theory is based on a continuum mechanical approach where dislocations are treated as field variables.

The objective of the ongoing development project is to reach a state where KRYP becomes a useful tool for predictions of grain interaction characteristics and texture formation properties in the process of developing new materials.

The code development project was initiated in August 2001.Today, six months later, KRYP is a fully functioning finite element program, including an FCC crystal plasticity model that is ready to be scrutinized in detail.

Keywords
crystal plasticity, meso-mechanics, continuum mechanics

Further bibliographic information

Language English

ISSN 1650-1942

Pages 30 p.

Price acc. to pricelist

Contents

1 Introduction 5

2 Governing Equations 6
- 2.1 Equations of Motion 6
- 2.2 Crystal Plasticity 6
  - 2.2.1 Kinematics 6
  - 2.2.2 Elastic Deformation 7
  - 2.2.3 Inelastic Deformation 7
  - 2.2.4 Objective Stress Update 7
- 2.3 Crystal Orientation 9
- 2.4 FCC Dislocation Density Model 11
  - 2.4.1 Dislocation Kinematics 11
  - 2.4.2 Dislocation Evolution Laws 12
  - 2.4.3 Slip Activation Stress 13
- 2.5 Grain Boundaries 13

3 Numerical Implementation 14
- 3.1 Element Formulation 14
- 3.2 Time Integration 14
- 3.3 Overall Structure 14

4 Benchmark Tests 16
- 4.1 Elastic Stress Pulse 16
- 4.2 Bar Impact 16
- 4.3 Aggregate of $8 \times 8 \times 8$ grains 20
  - 4.3.1 Test A 20
  - 4.3.2 Test B 20
  - 4.3.3 Test C 21
- 4.4 Texture 26
- 4.5 Crystal Orientation Control 28

5 Next Step 30

References 30

1 Introduction

The relationships between the micro-structure of an alloy and its mechanical properties are not always easily predicted. There are situations where one posseses a good knowledge about the properties of single grains in the structure, but not about their interaction characteristics.

The development of a simulation tool is motivated by the assumption that a carefully defined mathematical model will help bringing insight into the physics of grain interaction and texture formation.

One first has to choose an appropriate spatial scale of modelling. There are a few commonly applied methods to choose between.

A *molecular dynamics* model is suitable for studying the interaction between individual atoms, c.f. Horstemeyer et.al [1] and Hansen et.al [2]. With an interatomic spacing of a few tenths of a nanometer, a micrometer sized cube of material contains several billion atoms. Todays largest clusters of fast computers can not practically model even such a small piece of material.

In *dislocation dynamics* the corpuscular treatment of single atoms is abandoned, c.f. Rhee et al. [3]. Instead, the core material is modelled as an elastic continuum, into which the dislocations are embedded as explicitly described one-dimensional structures. A dislocation dynamics model is completed by assumptions regarding the dislocation activation stresses and their interaction properties. This approach readily allows the study of micrometer sized structures. However, defining the dislocation properties is not a trivial task.

KRYP works at an even larger spatial length scale. The theory is completely based based on continuum mechanics and crystal lattice defects are described by field variables. It is important to note that the approach is not well suited for studying the interaction between dislocations, inclusions and vacancies on a nanoscopic level. The code is developed for meso-mechanical simulations, where a typical model may consist of between 1 and 1000 grains. Each grain is normally modelled with between 1 and 10^4 finite elements.

2 Governing Equations

The mathematical model consists of the equations of motion, boundary conditions and of kinematical and constitutive relations.

2.1 Equations of Motion

In KRYP the acceleration field of a body is defined through the momentum balance equation, c.f. Gurtin [4].

$$\varrho \mathbf{a} - \mathrm{div}\boldsymbol{\sigma} - \mathbf{f} = \mathbf{0} \tag{1}$$

where $\varrho(\mathbf{x}, t)$ is the density, $\mathbf{a}(\mathbf{x}, t)$ is the acceleration vector and $\boldsymbol{\sigma}(\mathbf{x}, t)$ is the Cauchy stress tensor. $\mathbf{f}(\mathbf{x}, t)$ represents external body forces, such as gravity or magnetic forces. $\mathbf{x}$ is a spatial coordinate in space and t is the time.

The acceleration field can be integrated in time to deliver the velocity field, $\mathbf{v}(\mathbf{x}, t)$, and the displacement field, $\mathbf{d}(\mathbf{x}, t)$. The acceleration depends on the divergence of the current stress field. The stress state is material and deformation history dependent. Hence, a temporal solution to the momentum equation requires definitions of constitutive and kinematical relations.

2.2 Crystal Plasticity

The kinematics and the constitutive relations in KRYP are based on crystal plasticity theories, where plastic deformations are imposed by the activation of crystallographic glide planes.

The continuum approach of modeling naturally leads to a treatment of dislocations as field variables. This requires evolution laws, defining the formation and motion of dislocations.

2.2.1 Kinematics

The velocity gradient, $\mathbf{L}(\mathbf{x}, t)$, is defined as the sum of crystal slip, $\mathbf{L}^c(\mathbf{x}, t)$, the elastic strain rate, $\mathbf{D}^e(\mathbf{x}, t)$, and a rigid spin, $\mathbf{W}^r(\mathbf{x}, t)$.

$$\begin{aligned}
&\mathbf{L} = \frac{\partial \mathbf{v}}{\partial \mathbf{x}} = \mathbf{L}^c + \mathbf{L}^e \\
&\mathbf{L}^c = \mathbf{D}^c + \mathbf{W}^c \\
&\mathbf{L}^e = \mathbf{D}^e + \mathbf{W}^r \\
&\mathbf{L}^c = \sum_{i=1}^{M} \sum_{j=1}^{N} \dot{\alpha}_{ij} \hat{\mathbf{L}}^c_{ij} = \sum_{i=1}^{M} \sum_{j=1}^{N} \dot{\alpha}_{ij} \hat{\mathbf{t}}_{ij} \otimes \hat{\mathbf{n}}_j
\end{aligned} \tag{2}$$

$\hat{\mathbf{n}}_j$ is a glide plane normal and $\hat{\mathbf{t}}_{ij}$ is a glide plane slip direction ($\hat{\mathbf{t}}_{ij} \perp \hat{\mathbf{n}}_j$). For an FCC crystal $M = 3$ and $N = 4$. Further, $\hat{\mathbf{n}}_j$, $j = [1, N]$ are the four $\{1\ 1\ 1\}$-directions and $\hat{\mathbf{t}}_{ij}$, $(i, j) = [1, M] \times [1, N]$ are the corresponding orthogonal $< 1\ 1\ 0 >$-directions.

Observe that $\dot{\alpha}_{ij} = 0$ for a purely elastic deformation.

2.2.2 Elastic Deformation

The elastic respons of the material is assumed linear and isotropic. The Lie derivative $\boldsymbol{\sigma}^{\nabla}(\mathbf{x}, t)$, c.f. Belytschko et al. [5], of the Cauchy stress tensor $\boldsymbol{\sigma}(\mathbf{x}, t)$ is defined as

$$\boldsymbol{\sigma}^{\nabla} = \lambda \mathrm{tr}\mathbf{D}^e\, \mathbf{I} + 2\mu\mathbf{D}^e \tag{3}$$

where

$$\begin{aligned} \lambda &= \frac{\nu E}{(1+\nu)(1-2\nu)} \\ \mu &= \frac{E}{2(1+\nu)} \end{aligned} \tag{4}$$

E and ν are the Young's modulus and the Poisson's ratio, respectively.

2.2.3 Inelastic Deformation

According to Equation (2), the inelastic velocity gradient, $\mathbf{L}^c$, is a function of $\dot{\alpha}_{ij}$, $(i, j) = [1, M] \times [1, N]$. The slip system stress, τ_{ij}, determines the magnitude of $\dot{\alpha}_{ij}$.

$$\begin{aligned} &\dot{\alpha}_{ij} = \begin{cases} 0 & \text{if } |\tau_{ij}| \le \tau^y_{ij} \\ \dfrac{|\tau_{ij}| - \tau^y_{ij}}{c}\mathrm{sgn}(\tau_{ij}) & \text{if } |\tau_{ij}| > \tau^y_{ij} \end{cases} \\ &\tau_{ij} = \boldsymbol{\sigma}\hat{\mathbf{n}}_j \cdot \hat{\mathbf{t}}_{ij} \end{aligned} \tag{5}$$

τ^y_{ij} is the activation stress for slip direction $\hat{\mathbf{t}}_{ij}$ and it is assumed to be a function of the material properties and of history variables, such as the dislocation densities and the temperature. c is a viscosity.

The rheological model of a single slip system is shown in Figure 1.

2.2.4 Objective Stress Update

The Cauchy stress, $\boldsymbol{\sigma}$, is a spatial tensor. Observer independency requires an objective update of the stress components due to rigid body rotations.

KRYP uses the computationally efficient Jaumann stress rate, c.f. Belytschko et al. [5]. The rigid spin tensor, $\mathbf{W}^r$, is assumed defining the rate of rigid body rotation. This is not very accurate at large strains and it is a potential source of errors.

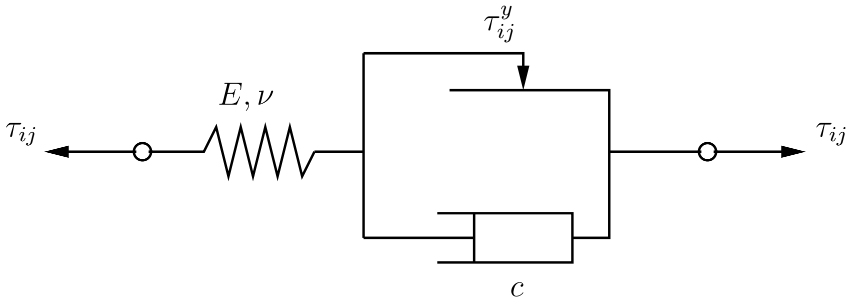

Figure 1: Rheological Model of a Slip System

$$\dot{\boldsymbol{\sigma}} = \boldsymbol{\sigma}^{\nabla} + \mathbf{W}^r\boldsymbol{\sigma} - \boldsymbol{\sigma}\mathbf{W}^r \tag{6}$$

It should be noted that $\mathbf{W}^r$ is not equivalent to the total spin, $\mathbf{W}$.

$$\mathbf{W} = \mathbf{W}^c + \mathbf{W}^r \tag{7}$$

It is assumed that spin due to plastic slip does not rotate the stress tensor. The assumption does not violate the objectivity and the author actually finds the idea physically appealing. A motivation based upon a deformation event is displayed in Figure 2, where a small material element is stretched and subsequently plastically deformed, such that $\mathbf{W}^c \neq \mathbf{0}$. The plastic deformation does not alter the direction of the elastic stretch. Consequently, $\boldsymbol{\sigma}$ should not spin due to a non zero $\mathbf{W}^c$.

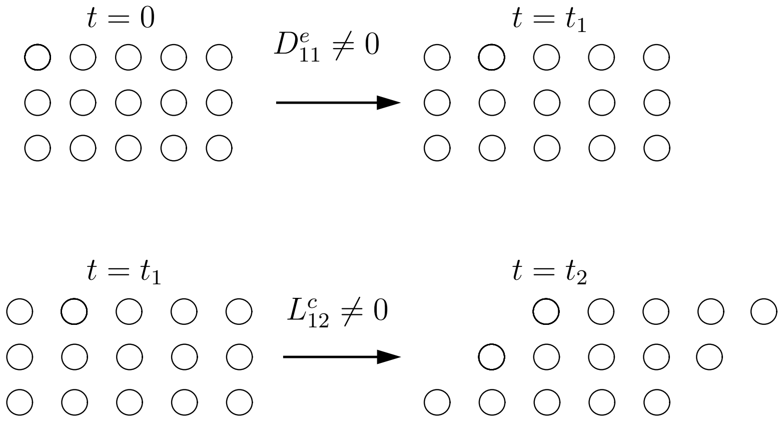

Figure 2: Deformation and plastic slip in a crystal.

2.3 Crystal Orientation

In abcense of twinning or sub-grain formation, the crystal orientation within a grain, $\mathcal{B}_g$, should only fluctuate due to variations in the elastic strain field. These elastically induced rotations are, for most practical applications, negligible.

The crystal orientation at a spatial coordinate, $\mathbf{x}_e \in \mathcal{B}_g$, is defined by three vectors, $\mathbf{c}_1(\mathbf{x}_e, t)$, $\mathbf{c}_2(\mathbf{x}_e, t)$ and $\mathbf{c}_3(\mathbf{x}_e, t)$. They point in the crystallographic $\{1\ 0\ 0\}$, $\{0\ 1\ 0\}$ and $\{0\ 0\ 1\}$-directions, respectively. The components of the vectors are stored in a tensor $\mathbf{C}(\mathbf{x}_e, t)$.

$$\begin{aligned} &\mathbf{C} = [C_{ij}] \\ &C_{ij}(\mathbf{x}_e, t) = c_{j,i}(\mathbf{x}_e, t) \end{aligned} \tag{8}$$

The crystal orientation, $\mathbf{C}(\mathbf{x}_e, t)$, will rotate due to any non-zero rigid spin tensor, $\mathbf{W}^r(\mathbf{x}_e, t)$.

$$\dot{\mathbf{C}} = \mathbf{W}^r \mathbf{C} \tag{9}$$

There is nothing in the kinematical relations preventing a non-uniform $\mathbf{W}^r$ and hence, the development of a non-uniform crystal orientation. Preserving a uniform crystal orientation within each grain requires special attention. The method introduced below focuses on a local suppression of those glide systems increasing the error in crystal orientation. This can be achieved by defining an orientation error dependent slip system activation stress, τ^y_{ij}.

The plan is to first define a measure of orientation error. Secondly, plastic slip increasing the error will be supressed to a certain degree. The chosen measure of the orientation error is based on the difference between the local and the grain average crystal orientation. The average crystallographic directions, $\bar{\mathbf{c}}_j, j = [1, 3]$, in $\mathcal{B}_g$ are defined as

$$\begin{aligned} &\bar{\mathbf{c}}_1 = \int_{\mathcal{B}_g} \mathbf{c}_1(\mathbf{x}, t) \mathrm{d}\mathcal{B}_g \Big/ \left| \int_{\mathcal{B}_g} \mathbf{c}_1(\mathbf{x}, t) \mathrm{d}\mathcal{B}_g \right| \\ &\hat{\mathbf{c}}_2 = \int_{\mathcal{B}_g} \mathbf{c}_2(\mathbf{x}, t) \mathrm{d}\mathcal{B}_g \Big/ \left| \int_{\mathcal{B}_g} \mathbf{c}_2(\mathbf{x}, t) \mathrm{d}\mathcal{B}_g \right| \\ &\bar{\mathbf{c}}_3 = \bar{\mathbf{c}}_1 \times \hat{\mathbf{c}}_2 \\ &\bar{\mathbf{c}}_2 = \bar{\mathbf{c}}_3 \times \bar{\mathbf{c}}_1 \end{aligned} \tag{10}$$

The definition above ensures an orthogonal tensor $\bar{\mathbf{C}}$.

$$\begin{aligned} &\bar{\mathbf{C}} = [\bar{C}_{ij}] \\ &\bar{C}_{ij} = \bar{c}_{j,i} \end{aligned} \tag{11}$$

The measure of error, $e(\mathbf{x}_e)$, is defined as

$$\begin{aligned} e = \ & (\bar{\mathbf{C}} - \mathbf{C}) : (\bar{\mathbf{C}} - \mathbf{C}) = \\ & \mathrm{tr}\left[(\bar{\mathbf{C}} - \mathbf{C})^{\mathrm{t}}(\bar{\mathbf{C}} - \mathbf{C})\right] = 6 - 2\mathrm{tr}\left[\bar{\mathbf{C}}^{\mathrm{t}}\mathbf{C}\right] \geq 0 \end{aligned} \tag{12}$$

It is now possible to check if the activation of a specific glide direction, $\hat{\mathbf{t}}_{ij}$, will increase or decrease the error. Knowing $\mathbf{v}(\mathbf{x})$ and consequently also $\mathbf{W}$ and $\mathbf{L}$,

$$\begin{aligned} \mathbf{W}^r = \ & \mathbf{W} - \mathbf{W}^c = \\ & \mathbf{W} - \frac{1}{2}\sum_{i=1}^{M}\sum_{j=1}^{N}\dot{\alpha}_{ij}\left[\hat{\mathbf{L}}_{ij}^c - (\hat{\mathbf{L}}_{ij}^c)^{\mathrm{t}}\right] \end{aligned} \tag{13}$$

Equation (13) displays how the activation of a specific glide system influences the rigid spin $\mathbf{W}^r$. The direction of spin, due to the activation of a specific glide system is

$$\frac{\partial \mathbf{W}^r}{\partial \dot{\alpha}_{ij}} = -\frac{1}{2}\left[\hat{\mathbf{L}}_{ij}^c - (\hat{\mathbf{L}}_{ij}^c)^{\mathrm{t}}\right] \tag{14}$$

Equations (9) and (14) give

$$\frac{\partial \dot{\mathbf{C}}}{\partial \dot{\alpha}_{ij}} = \frac{\partial \mathbf{W}^r}{\partial \dot{\alpha}_{ij}}\mathbf{C} = -\frac{1}{2}\left[\hat{\mathbf{L}}_{ij}^c - (\hat{\mathbf{L}}_{ij}^c)^{\mathrm{t}}\right]\mathbf{C} \tag{15}$$

Combining this expression with Equation (12),

$$\frac{\partial \dot{e}}{\partial \dot{\alpha}_{ij}} = -2\mathrm{tr}\left[\bar{\mathbf{C}}^{\mathrm{t}}\frac{\partial \dot{\mathbf{C}}}{\partial \dot{\alpha}_{ij}}\right] = \mathrm{tr}\left[\bar{\mathbf{C}}^{\mathrm{t}}\left[\hat{\mathbf{L}}_{ij}^c - (\hat{\mathbf{L}}_{ij}^c)^{\mathrm{t}}\right]\mathbf{C}\right] \tag{16}$$

The expression for $\partial\dot{e}/\partial\dot{\alpha}_{ij}$ is used to directly scale the glide plane activation stress, τ_{ij}^y.

$$\begin{aligned} & \tau_{ij}^y = Q_{ij}\hat{\tau}_{ij}^y \\ & Q_{ij} = 1 + Q_0 \max(0, \frac{\partial \dot{e}}{\partial \dot{\alpha}_{ij}} \cdot \mathrm{sgn}(\tau_{ij})) = \\ & \qquad 1 + Q_0 \max(0, \mathrm{tr}\left[\bar{\mathbf{C}}^{\mathrm{t}}\left[\hat{\mathbf{L}}_{ij}^c - (\hat{\mathbf{L}}_{ij}^c)^{\mathrm{t}}\right]\mathbf{C}\right] \cdot \mathrm{sgn}(\tau_{ij})) \end{aligned} \tag{17}$$

$\hat{\tau}_{ij}^y$ is the unscaled activation stress and Q_0 is a material parameter. Note that e is quadratic in $\mathbf{C} - \bar{\mathbf{C}}$. As a consequence Q_{ij} is linear in $\mathbf{C} - \bar{\mathbf{C}}$. This is highly important, as small orientational errors will not significantly stiffen the system.

2.4 FCC Dislocation Density Model

In a first test model the glide plane yield stresses are simply defined as functions of the dislocation densities. The model has been built to qualitatively capture some grain size effects.

2.4.1 Dislocation Kinematics

The total dislocation density, $\rho(\mathbf{X}, t)$, is the sum of immobile, $\rho^I(\mathbf{X}, t)$, and mobile, $\rho^M(\mathbf{X}, t)$, densities. $\mathbf{X}$ denotes a material coordinate.

$$\rho = \rho^I + \rho^M \tag{18}$$

The mobile dislocation density is further split into eight groups according to

$$\rho^M = \sum_{j=1}^{4} \rho_j^+ + \sum_{j=1}^{4} \rho_j^- \tag{19}$$

ρ_j^+ and ρ_j^- are densities of dislocations that move in directions orthogonally to glide plane normal $\hat{\mathbf{n}}_j$. ρ_j^+ and ρ_j^--dislocations are geometrically different and they are, for a certain slip rate $\dot{\alpha}_{ij}$, bound to move in opposite directions. This is schematically visualized in Figure 3.

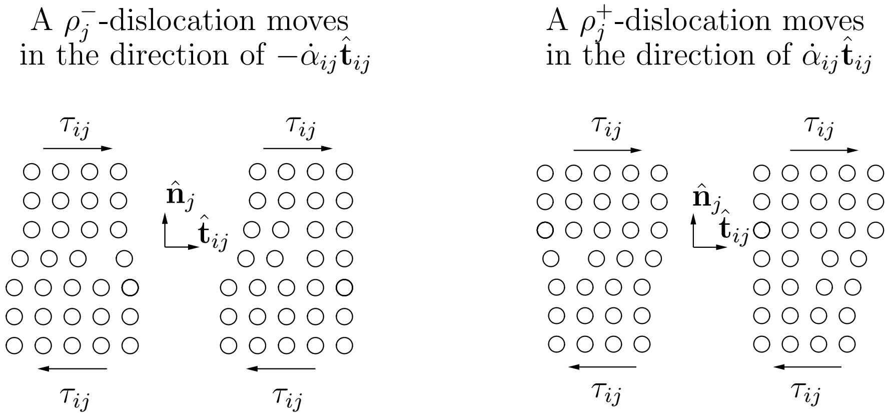
A ρ_j^--dislocation moves in the direction of $-\dot{\alpha}_{ij}\hat{\mathbf{t}}_{ij}$

A ρ_j^+-dislocation moves in the direction of $\dot{\alpha}_{ij}\hat{\mathbf{t}}_{ij}$

Figure 3: Dislocations moving through the lattice.

There is an assumed direct relationship between the flux of dislocations and the developed rate of gliding, $\dot{\alpha}_{ij}$.

$$\begin{aligned} \dot{\alpha}_{ij} &= \dot{\alpha}_{ij}^+ + \dot{\alpha}_{ij}^- \\ \dot{\alpha}_{ij}^+ &= b\rho_j^+ \bar{v}_{ij}^+ \\ \dot{\alpha}_{ij}^- &= -b\rho_j^- \bar{v}_{ij}^- \end{aligned} \tag{20}$$

b is Burger's vector. $\bar{v}_{ij}^+$ and $\bar{v}_{ij}^-$ are the average flux velocities of ρ_j^+ and ρ_j^--dislocations moving in the $\hat{\mathbf{t}}_{ij}$ slip direction, respectively.

2.4.2 Dislocation Evolution Laws

The evolution of the total dislocation density is governed by the production of new dislocations and by the dislocation flux.

$$\dot{\rho} = \dot{\rho}^p + \dot{\rho}^f \tag{21}$$

The dislocation production is defined as

$$\dot{\rho}^p = (z_3 - z_4 \rho)\sqrt{\mathbf{L}^c : \mathbf{L}^c} \tag{22}$$

z_3 and z_4 are constants. The flux arises from slip induced motion of mobile dislocations.

$$\dot{\rho}^f = \sum_{j=1}^{N} \left(\dot{\rho}_j^{f+} + \dot{\rho}_j^{f-} \right) \tag{23}$$

where

$$\begin{aligned} \dot{\rho}_j^{f+} &= \sum_{i=1}^{M} \boldsymbol{\nabla} \left(\rho_j^{+} \bar{v}_{ij}^{+} \right) \cdot \hat{\mathbf{t}}_{ij} = \frac{1}{b} \sum_{i=1}^{M} \boldsymbol{\nabla} \dot{\alpha}_{ij}^{+} \cdot \hat{\mathbf{t}}_{ij} \\ \dot{\rho}_j^{f-} &= -\sum_{i=1}^{M} \boldsymbol{\nabla} \left(\rho_j^{-} \bar{v}_{ij}^{-} \right) \cdot \hat{\mathbf{t}}_{ij} = -\frac{1}{b} \sum_{i=1}^{M} \boldsymbol{\nabla} \dot{\alpha}_{ij}^{-} \cdot \hat{\mathbf{t}}_{ij} \end{aligned} \tag{24}$$

Defining of the evolution of mobile dislocations completes the dislocation density evolution laws.

$$\begin{aligned} \dot{\rho}_j^{+} &= \dot{\rho}_j^{p+} + \dot{\rho}_j^{f+} \\ \dot{\rho}_j^{-} &= \dot{\rho}_j^{p-} + \dot{\rho}_j^{f-} \end{aligned} \tag{25}$$

where $\dot{\rho}_j^{p+}$ and $\dot{\rho}_j^{p-}$ are productions of mobile dislocations. The production is a combination of the creation of new dislocations, immoblization of exisiting mobile dislocations and remobilization of immobile dislocations. The production is assumed isotropic and it is defined as

$$\dot{\rho}_j^{p+} = \dot{\rho}_j^{p-} = \frac{1}{8} \left(z_5 \rho^I - z_6 \rho^M \right) \sqrt{\mathbf{L}^c : \mathbf{L}^c} \tag{26}$$

z_5 and z_6 are constants.

Having the total and the mobile dislocation density evolutions defined, the evolution the immobile dislocation density becomes

$$\dot{\rho}^I = \dot{\rho} - \dot{\rho}^M = (z_3 - z_4 \rho - z_5 \rho^I + z_6 \rho^M)\sqrt{\mathbf{L}^c : \mathbf{L}^c} \tag{27}$$

2.4.3 Slip Activation Stress

There are two activations stresses for each glide mechanism, τ_{ij}^{y+} and τ_{ij}^{y-}. They refer to the stresses necessary to activate the motion of the ρ_j^+ and ρ_j^- dislocations, respectively.

$$\begin{aligned}\tau_{ij}^{y+} &= \tau_0^y \left(z_1 + (1-z_1)\sqrt{\frac{\rho}{\rho_0}} \right) \left(z_2 + (1-z_2)\frac{\rho_0^M}{8\rho_j^+} \right) Q_{ij} \\ \tau_{ij}^{y-} &= \tau_0^y \left(z_1 + (1-z_1)\sqrt{\frac{\rho}{\rho_0}} \right) \left(z_2 + (1-z_2)\frac{\rho_0^M}{8\rho_j^-} \right) Q_{ij}\end{aligned} \tag{28}$$

z_1, z_2, ρ_0, ρ_0^M and τ_0^y are material constants. Following the relations in Equations (2) and (20),

$$\mathbf{L}^c = \sum_{i=1}^{M}\sum_{j=1}^{N}\dot{\alpha}_{ij}\bar{\mathbf{L}}_{ij}^c = \sum_{i=1}^{M}\sum_{j=1}^{N}\left(\dot{\alpha}_{ij}^+ + \dot{\alpha}_{ij}^-\right)\hat{\mathbf{t}}_{ij}\otimes\hat{\mathbf{n}}_j \tag{29}$$

where

$$\begin{aligned}\dot{\alpha}_{ij}^+ &= \begin{cases} 0 & \text{if } |\tau_{ij}| \le \tau_{ij}^{y+} \\ \dfrac{|\tau_{ij}| - \tau_{ij}^{y+}}{c}\operatorname{sgn}(\tau_{ij}) & \text{if } |\tau_{ij}| > \tau_{ij}^{y+} \end{cases} \\ \dot{\alpha}_{ij}^- &= \begin{cases} 0 & \text{if } |\tau_{ij}| \le \tau_{ij}^{y-} \\ \dfrac{|\tau_{ij}| - \tau_{ij}^{y-}}{c}\operatorname{sgn}(\tau_{ij}) & \text{if } |\tau_{ij}| > \tau_{ij}^{y-} \end{cases}\end{aligned} \tag{30}$$

2.5 Grain Boundaries

Grain boundary charateristics and criterias for dislocations propagating to adjacent grains are not yet taken into account in KRYP.

3 Numerical Implementation

KRYP is written in Fortran 90. The code outputs ascii files containing geometry and connectivity information, nodal velocities and element history variables. MATLAB is used for visualization of the results.

3.1 Element Formulation

The program only works with eight-noded selectively reduced integrated brick elements, where deviatoric stresses are computed at eight integration points per element. The pressure is sampled at the center of each brick, c.f. Hughes [6].

Since volmetric strains are only evaluated at the element centers local inversion of the material is numerically possible. Material inversion at deviatoric integration points likely leads to bad results or to no results at all.

KRYP uses a technique where deviatoric integration points are moved towards the element center whenever the material is in danger of inverting.

3.2 Time Integration

The 2$^{\mathrm{nd}}$ order accurate central difference finite difference scheme is applied for the time integration. The scheme is explicit and conditionally stable, c.f. Hughes [6].

$$\begin{array}{lcl} \ddot{\mathbf{Y}}^{n} & = & \mathbf{M}^{-1}(\mathbf{F}^{int} + \mathbf{F}^{ext}) \\ \dot{\mathbf{Y}}^{n+\frac{1}{2}} & = & \dot{\mathbf{Y}}^{n-\frac{1}{2}} + \ddot{\mathbf{Y}}^{n}\Delta t \\ \mathbf{Y}^{n} & = & \mathbf{Y}^{n-1} + \dot{\mathbf{Y}}^{n+\frac{1}{2}}\Delta t \end{array} \tag{31}$$

$\mathbf{Y}^n$ is the global node displacement vector at time increment n. $\mathbf{M}$ is a lumped mass matrix, a diagonal matrix of nodal masses. Δt is the time step size and $\mathbf{F}^{int}$ and $\mathbf{F}^{ext}$ are the internal and external nodal force vectors, respectively.

3.3 Overall Structure

The program flow and the time integration loop is depicted with a flow chart in Figure 4, where Δt^{out} is the time interval for writing geometry, stress and history variable data to the disk.

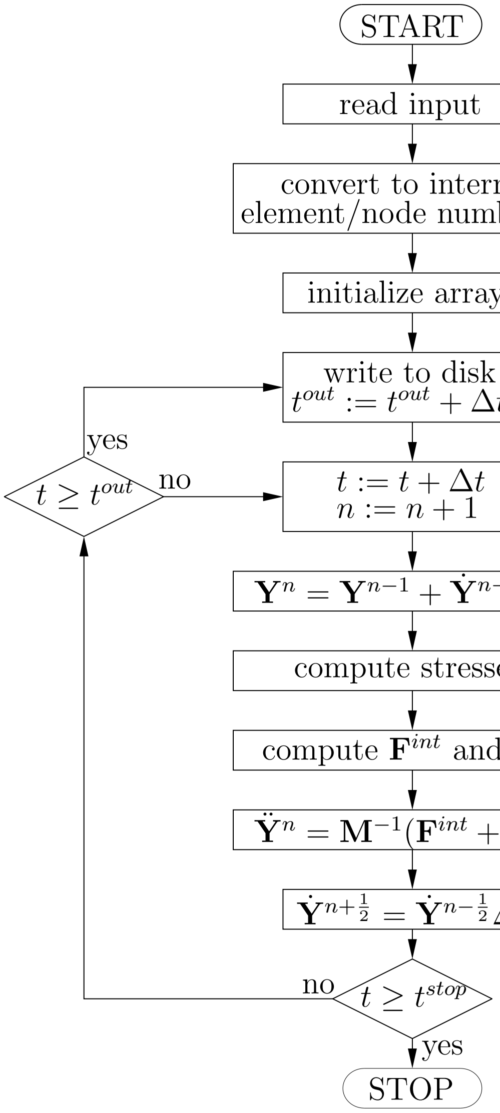

Figure 4: Internal structure of KRYP

4 Benchmark Tests

A few of benchmark tests have been designed for verification of the code. The validation of the program is a continuously ongoing process and extensive further testing is necessary.

4.1 Elastic Stress Pulse

The treatment of elastic deformations has been tested in a model of a stress pulse propagating through a circular bar. The pulse was generated by specifying an initial axial velocity of $10\,m/s$ at the first $0.1\,m$ of the bar, see Figure 5.

The respons of an element located on the material surface, $1.0\,m$ from both ends of the bar, was compared to results obtained with LS-DYNA. Figure 6 shows the axial stress history of the element.

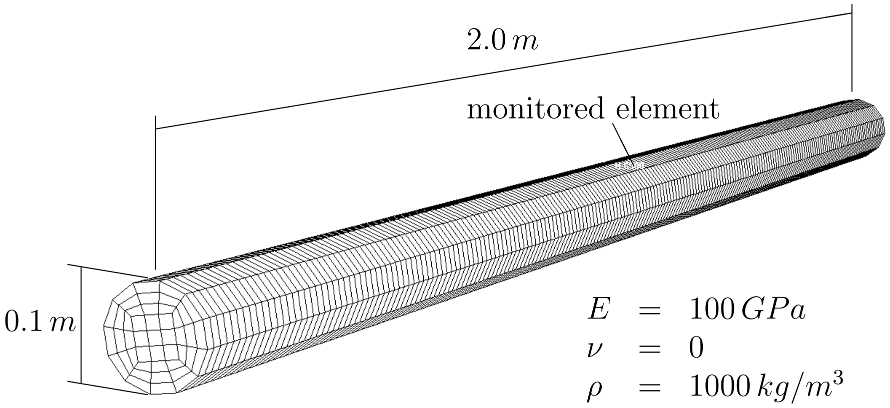

Figure 5: Elastic bar in pressure pulse benchmark test

4.2 Bar Impact

KRYP is equipped with an isotropic elasto-plastic constitutive model with linear plastic hardening. The effective stress is according to von Mises and the plastic flow is assumed associated.

$$\sigma_y = \sigma_0 + H \cdot \varepsilon^p_{eff} \tag{32}$$

where σ_y is the yield stress, σ_0 it the initial yield stress, H is a hardening parameter and ε^p_{eff} is the effective plastic strain.

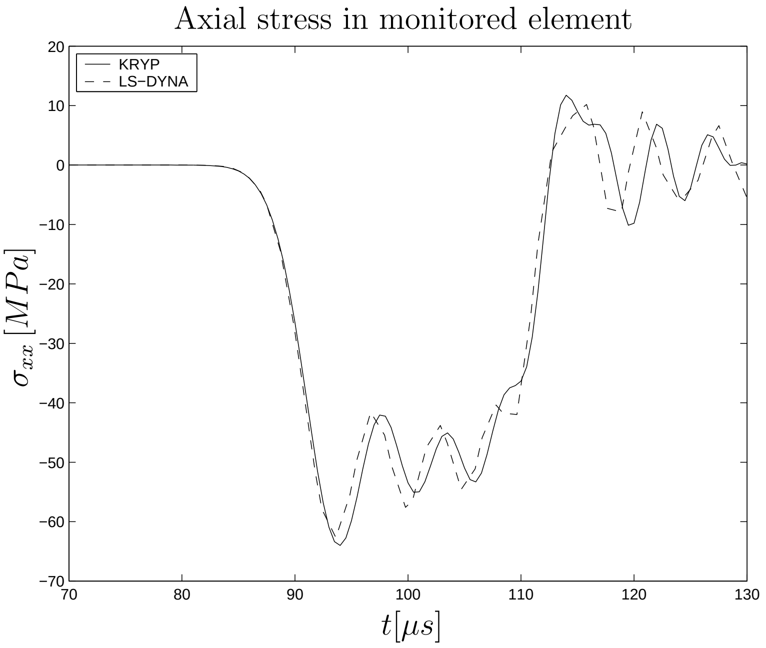

Figure 6: Registered data in pressure pulse benchmark test

LS-DYNA has no constitutive laws based on crystal plasticity. The isotropic elasto-plastic model was implemented in KRYP to allow for more extensive comparisons between the two codes.

The treatment of isotropic plasticity has been put to the test in a model of a metal bar impacting a rigid wall at a velocity of $200\,m/s$, see Figure 7. The displacement history of a node and the effective plastic strain of an element were recorded, see Figure 8.

Both KRYP and LS-DYNA were running with eight point selectively integrated elements and with a constant time step $\Delta t = 0.25\,\mu s$. The discrepancy between the codes is to some extent related to different contact stiffnesses.

Material 1

$$\begin{aligned} \sigma_0 &= 5\,MPa \\ H &= 100\,MPa \\ E &= 100\,GPa \\ \nu &= 0.3 \\ \rho &= 1000\,kg/m^3 \end{aligned}$$

Material 2

$$\begin{aligned} \sigma_0 &= 25\,MPa \\ H &= 100\,MPa \\ E &= 100\,GPa \\ \nu &= 0.3 \\ \rho &= 1000\,kg/m^3 \end{aligned}$$

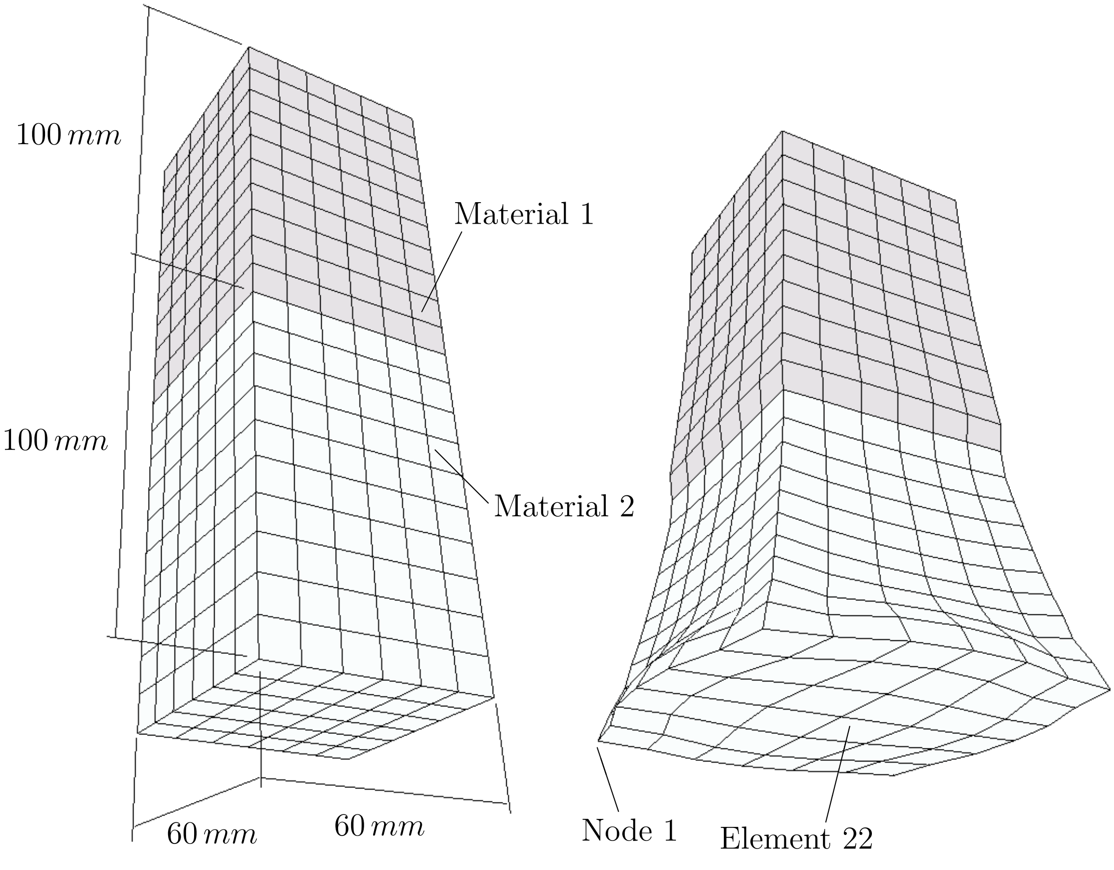

Figure 7: Metal bar impacting a rigid wall at $200\,m/s$.

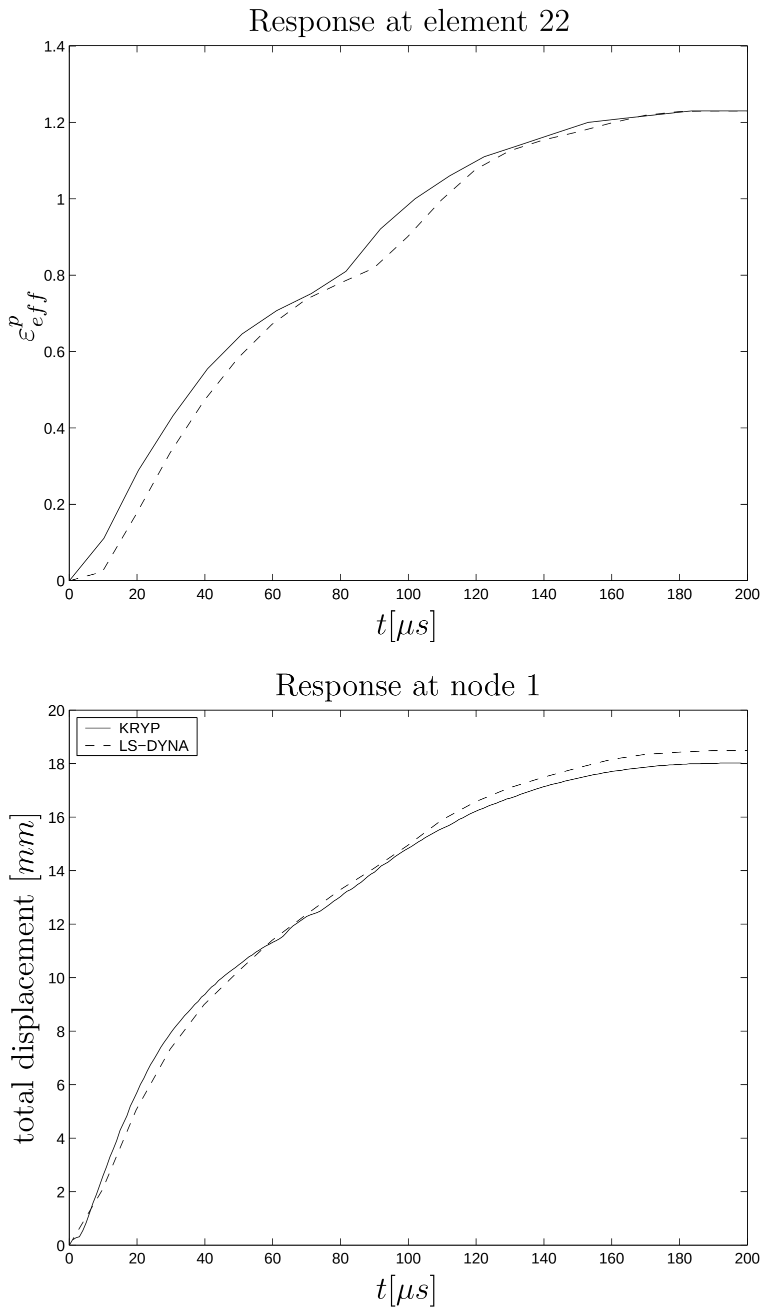

Figure 8: Registered data in metal bar impact simulation.

4.3 Aggregate of $8 \times 8 \times 8$ grains

Some characteristics of the, in Section 2.4, introduced FCC constitutive law have been tested on two $8 \times 8 \times 8$ cubic grain aggregates. The two aggregates were defined with $1.25\mu m$ and $12.5\mu m$ grains, respectively, and they were subjected to a uni-axial tension-compression history, see Figure 10.

The initial crystallographic {100}-directions were chosen parallell to the global x, y and z-axes.

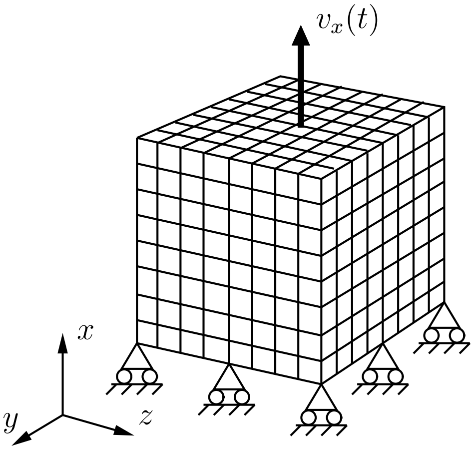

$E = 100\,GPa$
$\nu = 0.3$
$\rho_0 = 1.0 \cdot 10^8\,cm^{-2}$
$\rho_0^M = 1.0 \cdot 10^8\,cm^{-2}$
$\rho(0) = 1.0 \cdot 10^8\,cm^{-2}$
$\rho_j^{(+/-)}(0) = 1.25 \cdot 10^7\,cm^{-2}$
$\tau_0^y = 100\,MPa$
$b = 0.3\,nm$
$c = 100\,Pa\,s$
$z_1 - z_6 =$ see below

Figure 9: Uniaxial loading of a single grain.

4.3.1 Test A

In the first test z_1 and z_2 were set to 1. This leads to a constant glide plane yield stress.

$$\tau_{ij}^{y(+/-)} = \tau_0^y \tag{33}$$

The stress strain curve from deforming the $12.5\,\mu m$ aggregate is presented in Figure 11. The strain hardening effects are related to the formation of a chrystallographic texture.

4.3.2 Test B

Further strain hardening effects were introduced by setting $z_1 = 0$, $z_2 = 1$, $z_3 = 1 \cdot 10^9\,cm^{-2}$, $z_4 = 1$ and $z_5 = z_6 = 0$. z_3 and z_4 ensured the production of new dislocations and $z_1 = 0$ gave a glide plane yield stress according to

$$\tau_{ij}^{y(+/-)} = \tau_0^y \sqrt{\frac{\rho}{\rho_0}} \tag{34}$$

Once more the $12.5\,\mu m$ aggregate was tested, see Figure 12.

4.3.3 Test C

Finally, the yield stress function was modified to include mobile dislocation density effects. By setting $z_2 = 0$ and copying the remaining parameters from Test B, one obtained

$$\tau_{ij}^{y(+/-)} = \tau_0^y \sqrt{\frac{\rho}{\rho_0}} \sqrt{\frac{\rho_0^M}{8\rho_j^{(+/-)}}} \tag{35}$$

For this set of parameters, both the $12.5\,\mu m$ and the $1.25\,\mu m$ grain aggregatres have been tested. The mobile dislocations quickly reached the boundary of the small grains, where they were immobilized. This explains the stiffer respons of the $1.25\,\mu m$ grain aggregate, see Figure 13.

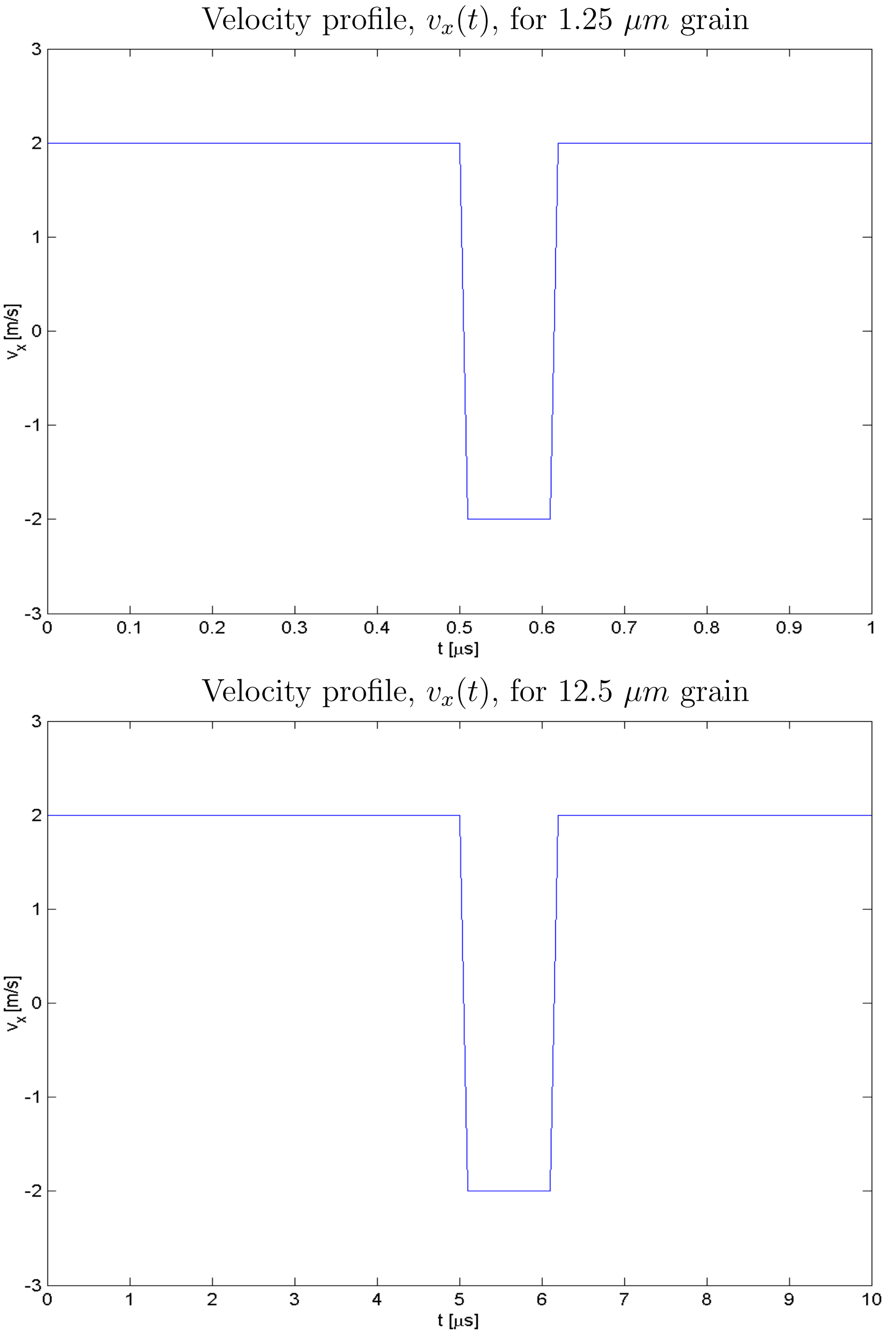

Velocity profile, $v_x(t)$, for 1.25 μm grain

Velocity profile, $v_x(t)$, for 12.5 μm grain

Figure 10: Prescribed tension/compression history in uni-axial tensile test.

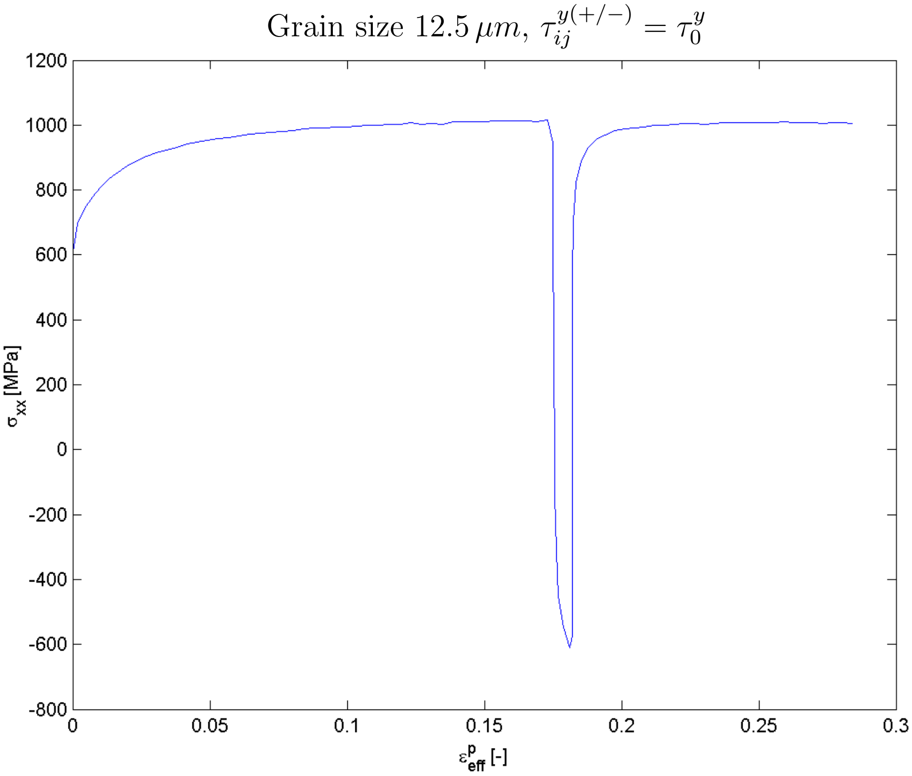

Figure 11: Stress-strain curve from Test A.

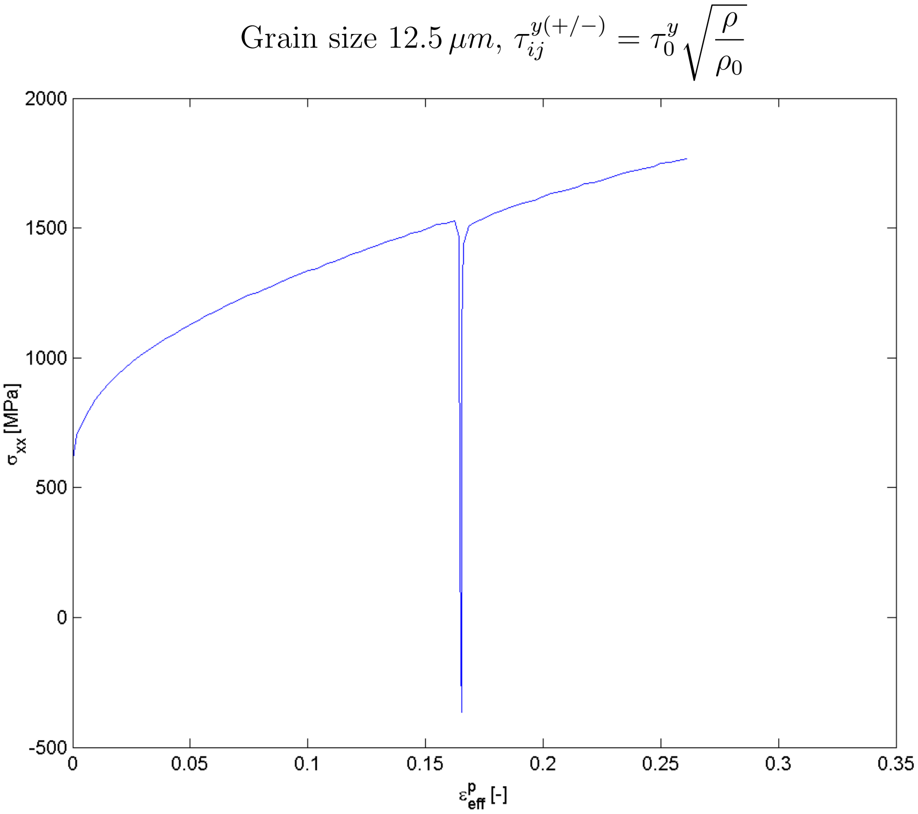

Figure 12: Stress-strain curve from Test B.

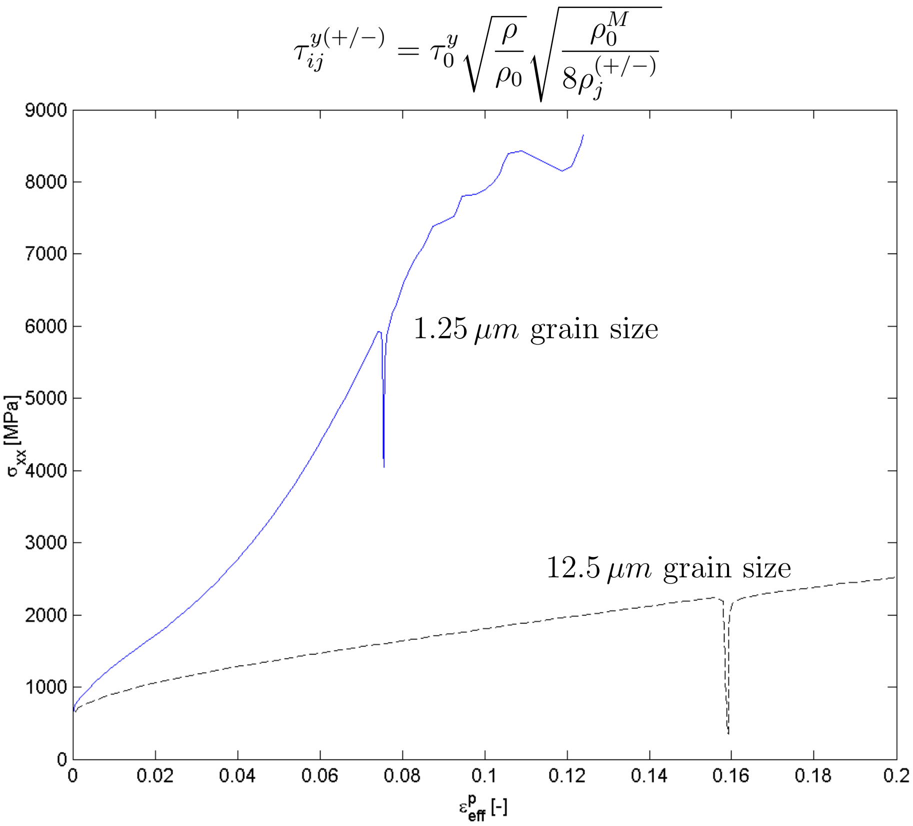

Figure 13: Stress-strain curve from Test C.

4.4 Texture

A texture evolution test has been performed by plastically deforming a model of $10 \times 10 \times 1$ cubic one-element grains under plane strain conditions, see Figure 14. Each cube had the initial size of $10\,\mu m$. The constitutive data were picked without any deeper thoughts. Figure 15 contains stereographic projections of the four $\{111\}$-directions in the initial and final configurations.

$$\begin{array}{lcllcl}
E & = & 100\,GPa & z_1 & = & 0.5 \\
\nu & = & 0.3 & z_2 & = & 0.5 \\
\rho_0 & = & 3.0 \cdot 10^{12}\,cm^{-2} & z_3 & = & 0.0 \\
\rho_0^M & = & 1.5 \cdot 10^{12}\,cm^{-2} & z_4 & = & 0.0 \\
\rho(0) & = & 3.0 \cdot 10^{12}\,cm^{-2} & z_5 & = & 0.0 \\
\rho_j^{(+/-)}(0) & = & 1.875 \cdot 10^{11}\,cm^{-2} & z_6 & = & 0.0 \\
\tau_0^y & = & 100\,MPa & c & = & 1000\,Pa\,s \\
b & = & 0.3\,nm & & &
\end{array}$$

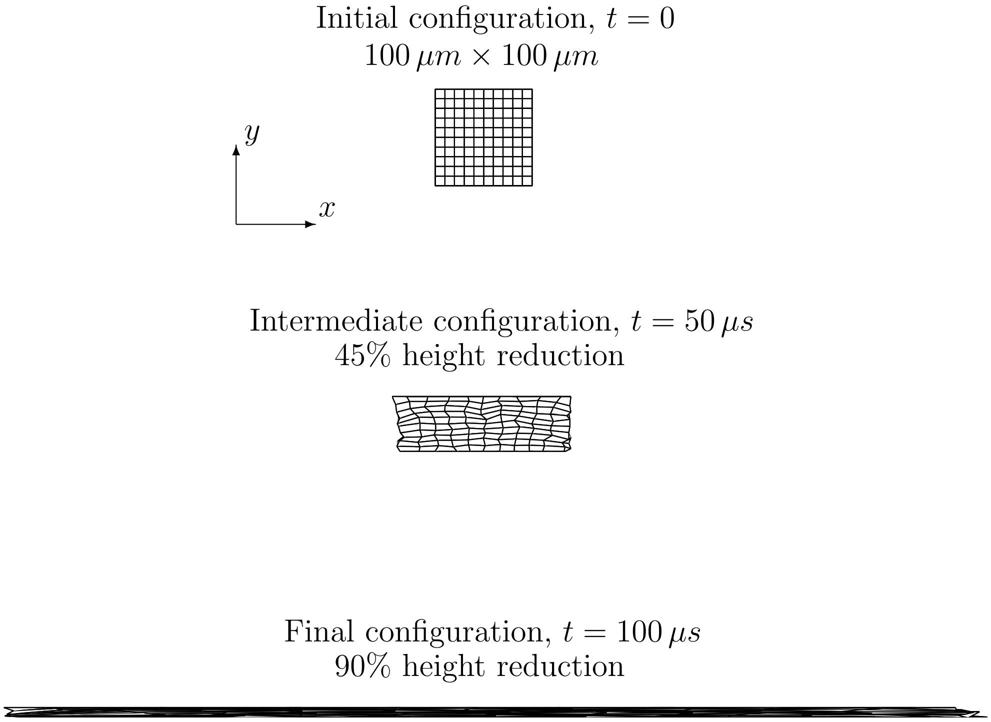

Figure 14: Compression of 100 initially cubic one-element grains.

Initial configuration, $t = 0$

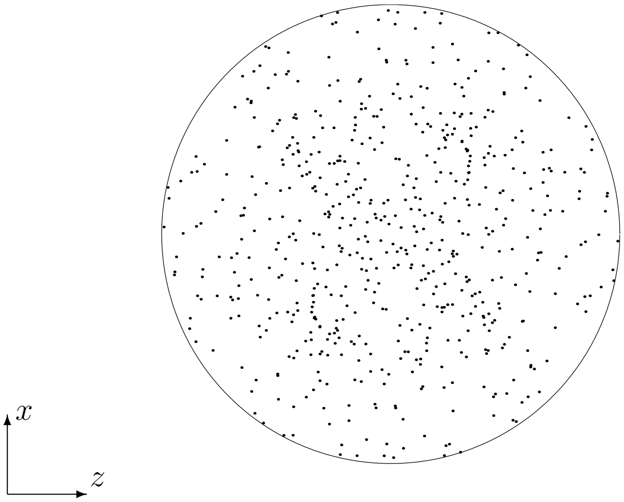

Final configuration, $t = 100\,\mu s$

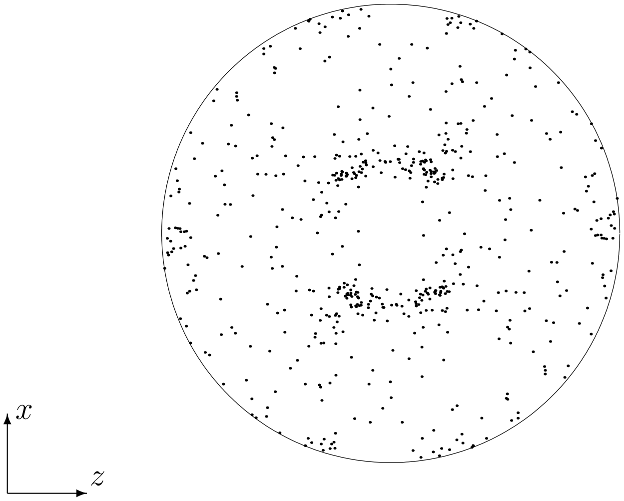

Figure 15: Pole figures showing the texture of the $\{111\}$-directions.

4.5 Crystal Orientation Control

A model of a rigid spherical punch indenting a single cubic grain resting on a friction free surface was set up to qualitatively examplify the effect of the non-local crystal orientation control, introduced in Section 2.3.

The punch had a diameter of $100\,\mu m$ and the indentation velocity and depth were $10\,m/s$ and $20\,\mu m$, respectively. The cubic grain, modeled with $8 \times 8 \times 8$ elements, had a size of $100\,\mu m$.

To minimize any effects of elastic strains, the grain was defined with a relatively small glide plane activation stress. The specifics of the model are shown in Figure 16. Figure 17 contains sterographic projections of the $\{111\}$-directions for simulations with and without the orientation control activated. Each element is represented by four points in the pole figures, one point for each crystallographic $\{111\}$-direction.

Even with a large non-zero Q_0 there are, unexpectedly, some elements significantly deviating from the average orientation. The problem needs to be analysed in more detail.

$E = 100\,GPa$
$\nu = 0.3$
$\rho_0 = 1.0 \cdot 10^{10}\,cm^{-2}$
$\rho_0^M = 1.0 \cdot 10^{10}\,cm^{-2}$
$\rho(0) = 1.0 \cdot 10^{10}\,cm^{-2}$
$\rho_j^{(+/-)}(0) = 1.25 \cdot 10^{9}\,cm^{-2}$
$\tau_0^y = 10\,MPa$
$b = 0.3\,nm$

$z_1 = 0.5$
$z_2 = 0.5$
$z_3 = 0.0$
$z_4 = 0.0$
$z_5 = 0.0$
$z_6 = 0.0$
$c = 10\,Pa\,s$
$Q_0 = [0, 10^4]$

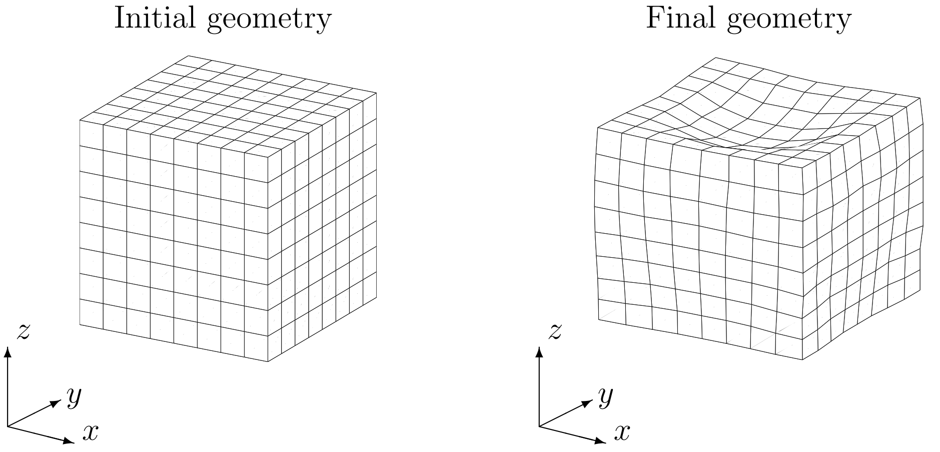

Figure 16: Spherical indentation in a single grain.

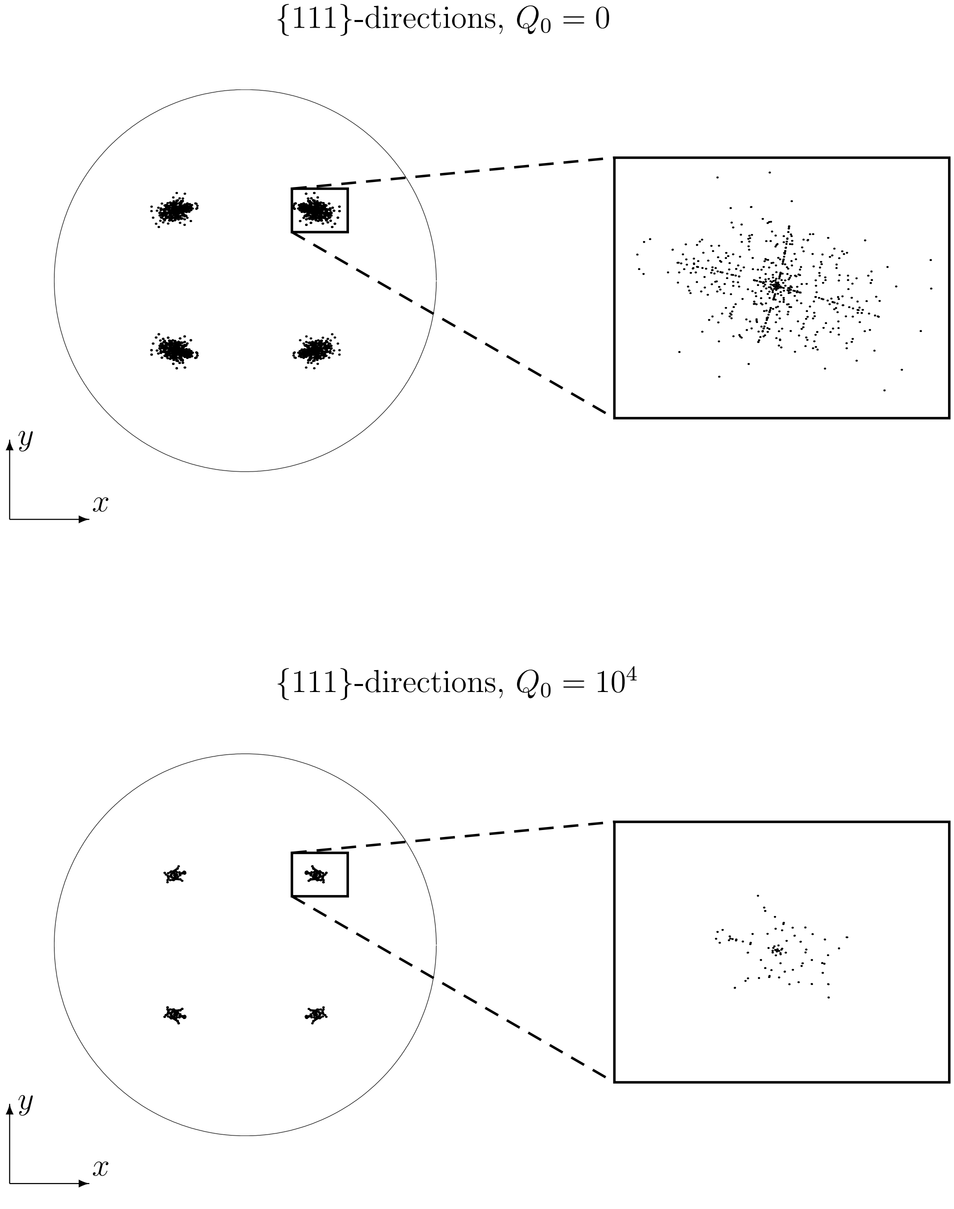

$\{111\}$-directions, $Q_0 = 0$

$\{111\}$-directions, $Q_0 = 10^4$

Figure 17: Stereographic projection after spherical indentation.

5 Next Step

There are certainly many functionalities missing in KRYP. Complex boundary conditions can hardly be defined, the code is not optimized for speed and there is no treatment of fracture. Eventually KRYP will need its own graphical interface for visualizing results and geometries. MATLAB is used for this purpose today, but it is a relatively expensive and slow software.

The list of important, but still not implemented, capabilities can be made longer. However, prior to the development of new functionalities it is suitable to proceed with the benchmarking and to try out the exisiting FCC model in comparisons with real experimental data.

It is the authors wish to optimize the material parameters against a set of well monitored uni- or bi-axial experiments on a one-phase FCC metal. The obtained set of parameters is to be used in the analysis of more complex processes, preferably at different grain sizes.

The outcoming of such a test would provide experience, helping out when staking out the course for the future of the project.

References

[1] M.F. Horstemeyer, M.I. Baskes and S.J. Plimpton, Computational nanoscale plasticity simulations using embedded atom potentials. *Theoretical and Applied Fracture Mechanics*, **37** (2001) 49-98.

[2] U. Hansen, P. Vogl, and V. Fiorentini. Quasiharmonic versus exact surface free energies of al: A systematic study employing a classical interatomic potential. *Physical Review B*, **60** (1999) 5055-5064.

[3] M Rhee, J.S. Stolken, V.V. Bulatov, T. Diaz de la Rubia, H.M. Zbib and J.P. Hirth. Dislocation stress fields for dynamic codes using anisotropic elasticity: methodology and analysis, *Materials Science and Engineering*, **A 309-310** (2001) 288-293.

[4] M.E. Gurtin, *An introduction to continuum mechanics.* Academic Press, Pittsburgh, 1981.

[5] T. Belytschko, W.K. Liu and B. Moran, *Nonlinear Finite Element for Continua and Structures.* John Wiley and Sons Ltd., Chichester, 2000.

[6] T.J.R. Hughes, *The Finite Element Method: Linear Static and Dynamic Finite Element Analysis.* Dover Publications Inc., Mineola, 2000.